Development of a Frequency-Adapted Virtual Fields Method as an alternative to the Corrected Force Analysis Technique for dynamic forces and structural parameter identification

Nicolas Madinier[a,b,1], Quentin Leclère[a], Kerem Ege[a] and Alain Berry[b]

[a]INSA Lyon, LVA, UR, 69621 Villeurbanne, France
[b]Centre de Recherche Acoustique - Signal - Humain, Université de Sherbrooke, 2500 Boulevard de l'Université, Sherbrooke (QC), CANADA

ABSTRACT

In vibroacoustics, inverse methods use the vibratory response of a structure to identify either a load or a structural parameter. The Force Analysis Technique (FAT) and the Virtual Fields Method (VFM), are two inverse methods that have been used in the past to identify loads or structural parameters of flexural beams or plates. The Corrected Force Analysis Technique (CFAT) is another inverse method that corrects the singularity of FAT, making this approach more accurate at higher frequencies. In this study, this principle is applied to the VFM, using polynomial interpolation of the displacement field, in order to adapt the method so that at each frequency, the accuracy of the method is improved. The accuracy of the Frequency-Adapted VFM is demonstrated using numerical simulations. A formal comparison between FAT, CFAT and the VFM is also proposed.

1. Introduction

In vibroacoustics, inverse methods are techniques used to fulfill different objectives. One of them is to identify a load, dynamic or not. Assuming that the material, geometry, and response of the structure to the unknown load are known, inverse methods can be applied to locate and quantify this force. A second important application is the determination of structural parameters such as bending stiffness or damping. Many inverse methods have been developed over the years. The main difference between them is the frequency range in which they are applicable. For example, if one wishes to identify the bending stiffness and damping in the low frequency domain, classical modal analysis can be used. Considering that the response of the structure is given by the sum of complex exponentials plus a Gaussian noise, the ESPRIT method can be used to perform modal analysis as long as the modal overlap remains below 70% [1]. In the high frequency range, ultrasonic methods can be applied [2]. In this paper, two medium frequency methods are used, the Force Analysis Technique or FAT and the Virtual Fields Method or VFM.

The Force Analysis Technique, developed in the 1990s [3, 4], is an inverse method whose initial objective is to identify a dynamic load. This method is based on the local equation of motion and allows to identify the load locally for flexural beams or plates. The local aspect of this method is one of its great advantages. Indeed, the technique can be applied without the need to know the conditions outside the region of interest such as the response and the boundary conditions of the structure or the material properties. FAT has been extended to identify the structural parameter for isotropic and homogeneous plates [5] and for more complex structures [6]. However, FAT is limited to the medium frequency domain. As the number of points per bending wavelength decreases (i.e. as frequency increases), the error of the method becomes significant [7, 8]. This limitation is overcome by the Corrected Force Analysis Technique or CFAT [8]. This method introduces factors (one for the case of a beam and two for a plate) to correct the estimate of the equation of motion made by FAT. More recently, CFAT has been extended to laminated composite panels [9]. This technique has also been applied to identify the structural parameter(s) of an isotropic [7], sandwich [10], and anisotropic [2] plate.

The Virtual Fields Method is a second inverse method based on the Principle of Virtual Works (PVW). This method uses test functions, also known as virtual fields, to solve the PVW [11]. The choice of the virtual fields is a key point of the VFM. The VFM has been applied in the past to identify a dynamic load in the frequency domain [12, 13] and in the time domain [14, 15]. Unlike FAT, the VFM was originally developed to identify structural parameter(s).

ORCID(s):
[1]nicolas.madinier@usherbrooke.ca

Nomenclature

a_p	Coefficients of the polynomial interpolating the displacement field
E	Young Modulus
E^{FAT}, E^{CFAT} and E^{VFM}	Response of FAT, CFAT and the VFM in the wavenumber domain
C_0, C_1 and C_2	Coefficients of the inertial term of $\tilde{p}^{\mathrm{VFM}}(x_i)$
I	Flexural moment of inertia
$k_f = 2\pi/\lambda_f = \sqrt[4]{\frac{\rho S}{EI}\omega^2}$	Flexural wavenumber of the beam
L	Length of the beam
l_v	Virtual segment
$n = \lambda_f/\Delta$	Number of measurement points by wavelength
N_r	Random variable sampled from a standard normal distribution
$p(x,t) = \tilde{p}(x)e^{j\omega t}$	Harmonic transverse loading in N/m
$\tilde{p}^{\mathrm{FAT}}(x_i)$, $\tilde{p}^{\mathrm{CFAT}}(x_i)$ and $\tilde{p}^{\mathrm{VFM}}(x_i)$	Load estimated by FAT, CFAT and the VFM at point x_i
$\hat{p}(k)$, $\hat{p}^{\mathrm{FAT}}(k)$ and $\hat{p}^{\mathrm{VFM}}(k)$	Fourier transform of $\tilde{p}(x)$, $\tilde{p}^{\mathrm{FAT}}(x)$ and $\tilde{p}^{\mathrm{VFM}}(x)$
S	Cross section of the beam
S_f	Noise sensitivity
U_0, U_1 and U_2	Multiplier coefficient for different displacement values in the load expression identified with FAT, CFAT and VFM
$\tilde{w}(x)$	Transverse displacement of the beam
$\hat{w}(k)$	Fourier transform of $\tilde{w}(x)$
$w^v(x)$	Virtual displacement
$W_M^{x_i}(\xi)$	Polynomial interpolating the displacement field measured on a subset of M points centered on the point with coordinates x_i
$\tilde{w}_{\mathrm{noisy}}(x)$	Noisy displacement
x_e	Position of the load
X_1 and X_2	Roots of the equation 28
η	Loss factor
$\delta_\Delta^{4x}(x_i)$	Estimation of the fourth-order spatial derivative of $\tilde{w}(x)$ by the finite differences scheme
δ_Δ^0, δ_Δ^x, δ_Δ^{2x} and δ_Δ^{3x}	Linear combination of the 5 measured displacement values of the subset used in the polynomial interpolation.
Δ	Distance between two measurement points
$\tilde{\kappa}_x(x) = -\frac{d^2\tilde{w}(x)}{dx^2}$	Bending curvature of the beam
$\kappa_x^v(x)$	Virtual curvature
$\kappa_{x\ M}^{x_i}(\xi) = -\frac{1}{\Delta^2}\frac{d^2W_M(\xi)}{d\xi^2}$	Curvatures are obtained by second-order derivation of $W_M^{x_i}(\xi)$
λ_f	Wavelength of the bending wave
$\mu^4 = \frac{\Delta^4 k_f^4}{(2-2\cos(k_f\Delta))^2}$	Corrective factor of CFAT
ρ	Density
$\xi = \frac{x-x_i}{\Delta}$	Local coordinate system on the virtual segment
τ	Virtual segment half-length
τ_{FA}	Frequency Adapted value of virtual segment half-length
σ_w	Standard deviation of the simulated displacement at ω
σ	Standard deviation σ of the identified structural parameter $EI/\rho S$
ω	Angular frequency

The method has therefore been applied to isotropic plates [16, 17], and to more complex structures [18, 19, 20, 21]. Work has been carried out to minimize the effects of measurement noise on the VFM by selecting specific virtual fields

which are referred to as optimized virtual fields [22]. These optimized virtual fields, which depend on the vibratory response of the structure, were tested to identify the structural parameters of a vibrating plate [23]. In 2017, Marek et al. extended these sensitivity-based VFM to identify the parameters of a plastic model [24]. In [25], viscoelastic material parameters were also estimated using optimal virtual fields and taking into account the biases introduced by spatial sampling in the experimental data. The VFM is based on a weak form of the local equilibrium while FAT is based on a strong form. Therefore, the VFM is considered less sensitive to measurement noise than FAT or CFAT [12]. However, the virtual fields have to be carefully chosen since they impact the accuracy of the VFM results. In this paper, the case of a beam in pure bending is considered. Using piecewise virtual fields and a polynomial interpolation of the displacement field, it is proposed to apply the principles that led to the FAT correction to the VFM in order to adapt the size of the virtual segment over which the piecewise virtual fields are defined. Like CFAT, the proposed VFM frequency adaptation is relevant when the number of measurement points per bending wavelength is low. In practice, this situation generally arises in the high-frequency range, when the vibration field is measured using laser vibrometry. The second section, presents the Force Analysis Technique and the Corrected Force Analysis Technique. The Principle of Virtual Works and the Virtual Fields Method are presented in the third section. The fourth section develops the frequency adaptation process of the Virtual Fields Method. Finally, a numerical simulation validation of the Frequency-Adapted Virtual Fields Method is presented in the fifth section.

2. Force Analysis Technique and Corrected Force Analysis Technique for loading and structural parameter identification

2.1. Force Analysis Technique

In this and the following sections, an Euler-Bernoulli beam of cross section S is considered. This beam is submitted to a harmonic transverse loading $p(x,t) = \tilde{p}(x)e^{j\omega t}$ (in N/m) where x denotes the position on the beam, ω the angular frequency and $\mathrm{j} = \sqrt{-1}$. The equation of motion of the beam is

$$EI\frac{d^4\tilde{w}(x)}{dx^4} - \rho S\omega^2\tilde{w}(x) = \tilde{p}(x), \tag{1}$$

where E, ρ and I are respectively the Young's modulus, the density and the flexural moment of inertia. Also, $\tilde{w}(x)$ is the transverse displacement of the beam. In FAT, the fourth-order spatial derivative of the displacement is estimated at $x = x_i$ using a finite difference scheme based on discrete experimental measurements of $\tilde{w}$. [8]:

$$\left.\frac{d^4\tilde{w}(x)}{dx^4}\right)_{x=x_i} \simeq \delta_\Delta^{4x}(x_i) = \frac{1}{\Delta^4}(\tilde{w}(x_i-2\Delta) - 4\tilde{w}(x_i-\Delta) + 6\tilde{w}(x_i) - 4\tilde{w}(x_i+\Delta) + \tilde{w}(x_i+2\Delta)). \tag{2}$$

Here, Δ is the distance between two measurement points. The load can then be estimated at the x_i position of the beam via :

$$\tilde{p}^{\mathrm{FAT}}(x_i) = EI\delta_\Delta^{4x}(x_i) - \rho S\omega^2\tilde{w}(x_i). \tag{3}$$

Estimating the fourth-order spatial derivative of $\tilde{w}(x)$ leads to an amplification of measurement noise, mainly in the high wavenumber domain. It is therefore necessary to apply a low-pass wavenumber filter on the experimental data to regularize the problem. In practice, to avoid Gibbs phenomenon, the identified force distribution is first spatially windowed and then low-pass filtered in the wavenumber domain [3]. A major issue when implementing FAT is that a strong bias error due to the finite difference approximation appears when the number of measurement points by wavelength, $n = \lambda_f/\Delta$, gets to small (practically, when $n < 4$). Note that here, $\lambda_f = 2\pi\sqrt[4]{\frac{EI}{\rho S\omega^2}}$ denotes the wavelength of the free bending wave.

2.2. Corrected Force Analysis Technique

The equation of motion of the Euler-Bernoulli beam in the wavenumber domain is,

$$\hat{p}(k) = \hat{w}(k)(EIk^4 - \rho S\omega^2), \tag{4}$$

where $\hat{p}(k)$ and $\iota\hat{w}(k)$ are the wavenumber transforms of $\tilde{p}(x)$ and $\iota\tilde{w}(x)$.
The wavenumber transform of eq. 3 is [8],

$$\hat{p}^{\mathrm{FAT}}(k) = \iota\hat{w}(k)\left(\frac{EI}{\Delta^4}(2\cos(2k\Delta) - 8\cos(k\Delta) + 6) - \rho S\omega^2\right). \tag{5}$$

The response of FAT in the wavenumber domain is quantified by the ratio of $\hat{p}^{\mathrm{FAT}}$ over $\hat{p}$,

$$E^{\mathrm{FAT}} = \frac{\hat{p}^{\mathrm{FAT}}}{\hat{p}} = \frac{\dfrac{2\cos(2k\Delta) - 8\cos(k\Delta) + 6}{\Delta^4} - k_f^4}{k^4 - k_f^4}, \tag{6}$$

where $k_f = \sqrt[4]{\frac{\rho S}{EI}\omega^2}$ is the flexural wavenumber of the beam. The response of FAT shows a singularity at $k = k_f$. In [8] it is proposed to remove this singularity by equalizing the roots of the denominator and the numerator of eq. 6. To do this, a factor μ^4 is introduced to correct the finite difference scheme for the estimation of force distribution,

$$\tilde{p}^{\mathrm{CFAT}}(x_i) = EI\mu^4\delta_\Delta^{4x}(x_i) - \rho S\omega^2\tilde{w}(x_i). \tag{7}$$

The corrected response is then,

$$E^{\mathrm{CFAT}} = \frac{\mu^4\dfrac{2\cos(2k\Delta) - 8\cos(k\Delta) + 6}{\Delta^4} - k_f^4}{k^4 - k_f^4}, \tag{8}$$

The value $\mu^4 = \frac{\Delta^4 k_f^4}{(2-2\cos(k_f\Delta))^2}$ equalizes the roots of the numerator and denominator, eliminating the singularity as intended. If the purpose is to identify a dynamic load, the CFAT method can be applied when the number of measurement points per bending wavelength is down to 1.85 [8]. Figure 5a shows the response of FAT and CFAT in the wavenumber domain for $n = 4$ and $n = 2.5$. The singularity at $k = k_f$ is clearly visible on the FAT plots while it is suppressed on the CFAT plots. The CFAT plot for $n = 2.5$ shows a second numerator root at $k/k_f = 1.5$. The FAT response includes a low-pass wavenumber filter which acts as an anti-aliasing filter. Indeed, Shannon's sampling criterion requires that $k/k_f < n/2$ [8]. As shown in figure 5a, the FAT response at $k/k_f = 2$ ($n = 4$) is -19 dB. Therefore, the identified force spectrum will not be distorted by aliasing effects. The same conclusion can be drawn for $n = 2.5$. One advantage of CFAT is that this anti-aliasing filter is preserved. Indeed, figure 5a shows that the CFAT response at $k/k_f = 2$ ($n = 4$) is -14 dB. The force spectrum of CFAT is then not disturbed by aliasing effects.

2.3. Structural parameter identification with FAT and CFAT

FAT and CFAT can also be used to estimate the structural parameter of the beam $EI/\rho S$ [5, 7]. The equation of motion of the Euler-Bernoulli beam at points where no external force is applied is,

$$EI\frac{d^4\tilde{w}(x)}{dx^4} - \rho S\omega^2\tilde{w}(x) = 0. \tag{9}$$

The fourth order spatial derivative can again be estimated by means of the finite difference scheme (corrected or not). The identified structural parameter is then :

$$\left(\frac{EI}{\rho S}\right)_{x_i}^{\mathrm{FAT}} = \frac{\omega^2\tilde{w}(x_i)}{\delta_\Delta^{4x}(x_i)}, \tag{10}$$

if FAT is used. Or

$$\left(\frac{EI}{\rho S}\right)_{x_i}^{\mathrm{CFAT}} = \frac{\omega^2\tilde{w}(x_i)}{\mu^4\delta_\Delta^{4x}(x_i)}, \tag{11}$$

if CFAT is used.

3. Virtual Fields Method for loading and structural parameter identification

The Virtual Fields Method is based on the Principle of Virtual Works (PVW) [11]. By multiplying both sides of eq. 1 by a function $w^v(x)$, and integrating along L, we get,

$$\int_L EI\frac{d^4\tilde{w}(x)}{dx^4}w^v(x)\mathrm{dx} - \int_L \rho S\omega^2\tilde{w}(x)w^v(x)\mathrm{dx} = \int_L \tilde{p}(x)w^v(x)\mathrm{dx}. \tag{12}$$

With specific properties of $w^v(x)$, a double integration by parts leads to the Principle of Virtual Works for an Euler-Benoulli beam,

$$EI\int_L \tilde{\kappa}_x(x)\kappa_x^v(x)\mathrm{dx} - \rho S\omega^2\int_L \tilde{w}(x)w^v(x)\mathrm{dx} = \int_L \tilde{p}(x)w^v(x)\mathrm{dx}, \tag{13}$$

where $\tilde{\kappa}_x(x) = -\frac{d^2\tilde{w}(x)}{dx^2}$ is the bending curvature of the beam, $w^v(x)$ and $\kappa_x^v(x)$ are the virtual displacement and the virtual curvature respectively. For the problem considered in this study, the virtual displacement can be any kinematically admissible function C^1 (continuity of the virtual displacement and its first derivative) along the length of the beam. This implies that the virtual displacement and its first spatial derivative have to be null at the boundary of the PVW integration domain. The Virtual Fields Method consists of choosing a virtual displacement in order to solve the PVW and identify the load $\tilde{p}(x)$ from the measured displacement field of the beam. Here, the virtual displacement is considered to be zero over the whole length of the beam except over a small segment called virtual segment which is centered at point $x = x_i$ [12]. Assuming that the external lineic force is constant over the virtual segment, the PVW becomes,

$$EI\int_{l_v} \tilde{\kappa}_x(x)\kappa_x^v(x)\mathrm{dx} - \rho S\omega^2\int_{l_v} \tilde{w}(x)w^v(x)\mathrm{dx} = \tilde{p}(x_i)\int_{l_v} w^v(x)\mathrm{dx}, \tag{14}$$

where l_v denotes the virtual segment. The position of this virtual segment changes to scan the entire beam. For each position, the PVW is solved and the load applied to the segment is identified. In order to respect the C^1 conditions on the virtual displacement, w^v and its first derivative must be zero at the ends of the virtual segment. As lineic force is considered constant over the virtual segment, the lineic force identified for a segment position is an average of the lineic force applied over the entire segment. Therefore, the integration on the right-hand side of eq.14 acts as a low-pass wavenumber filter, which helps to regularize the problem. Note that the VFM requires the knowledge of second spatial derivatives of the displacement (the curvatures κ), whereas FAT and CFAT require fourth-order spatial derivatives of displacements. In principle, this makes the VFM less sensitive to measurement noise on the displacement field.

3.1. Structural parameter identification with the VFM

The VFM can also be used to identify the structural parameter of the beam. If no external force is applied on l_v, the PVW becomes,

$$\left(\frac{EI}{\rho S}\right)_{x_i}^{\mathrm{VFM}} = \frac{\omega^2\int_{l_v}\tilde{w}(x)w^v(x)\mathrm{dx}}{\int_{l_v}\tilde{\kappa}_x(x)\kappa_x^v(x)\mathrm{dx}}. \tag{15}$$

The structural parameter can then be identified for each position of the virtual segment provided no external load is applied on the part of the beam covered by the successive virtual segments.

4. Frequency adaptation of the Virtual Fields Method

4.1. Polynomial interpolation of the displacement field

In this section, a set of N measurement points is considered over the whole length of the beam. Let us consider an odd number of M measurement points, which forms a sub-set of the N measurement points, as shown in the figure 1a. The knowledge of the displacement at each point of this subset is used to interpolate the displacements at any position by a polynomial function of degree $M-1$. So, if $x \in [x_i - \Delta\frac{M}{2}, x_i + \Delta\frac{M}{2}]$, then,

$$\tilde{w}(x) \simeq W_M^{x_i}(\xi) = \sum_{p=0}^{M-1} a_p\xi^p, \tag{16}$$

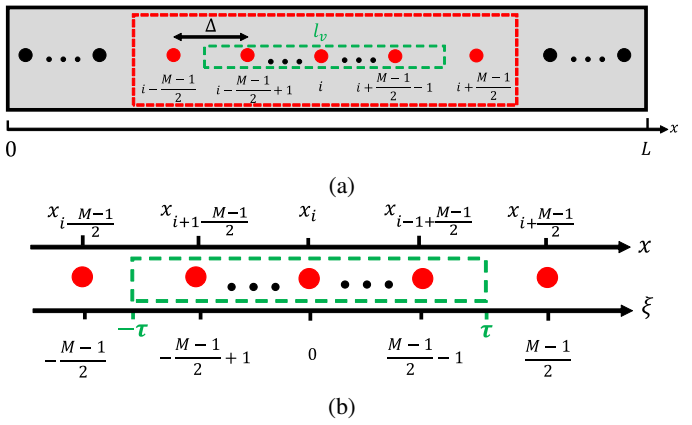

Figure 1: (a) Experimental mesh of N points spaced by Δ with the subset of M points. The virtual segment l_v is shown in green. (b) Coordinate systems on the subset of M points, x corresponding to global coordinates and ξ to local coordinates.

with $\xi = \frac{x-x_i}{\Delta}$, the local coordinate system on the virtual segment as shown in figure 1b. Here, the a_p are the coefficients of the polynomial. These coefficients depend on the displacement field and must be estimated. To do so the Newton formula is used [26],

$$W_M^{x_i}(\xi) = \sum_{v=1}^{M} \tilde{w}[\xi_1, ..., \xi_v] \prod_{s=1}^{v} (\xi - \xi_s). \tag{17}$$

Newton's formula uses the divided difference operator,

$$\begin{aligned} \tilde{w}[\xi_1] &= \tilde{w}(\xi_1), \\ \tilde{w}[\xi_1, \xi_2] &= \frac{\tilde{w}(\xi_1) - \tilde{w}(\xi_2)}{\xi_1 - \xi_2}, \\ \tilde{w}[\xi_1, ..., \xi_v] &= \frac{\tilde{w}[\xi_1, ..., \xi_{v-1}] - \tilde{w}[\xi_2, ..., \xi_v]}{\xi_1 - \xi_v}, \end{aligned} \tag{18}$$

where $\tilde{w}(\xi_v)$ is the measured displacement at node ξ_v. The curvatures are obtained by second-order derivation of eq. 17, $\kappa_{x\,M}^{x_i}(\xi) = -\frac{1}{\Delta^2}\frac{d^2 W_M(\xi)}{d\xi^2}$.

4.2. Virtual Fields Method for force identification with $M = 5$

The case where $M = 5$ is considered hereafter in order to remain consistent with the number of points used by FAT and CFAT for the estimation of $d^4\tilde{w}/dx^4$. In this case, the polynomial interpolation obtained with Newton's formula is,

$$W_5^{x_i}(\xi) = \frac{1}{24}\delta_\Delta^{4x}\xi^4 + \frac{1}{72}\delta_\Delta^{3x}\xi^3 + \left(\frac{1}{14}\delta_\Delta^{2x} - \frac{31}{168}\delta_\Delta^{4x}\right)\xi^2 + \left(\frac{1}{10}\delta_\Delta^{x} - \frac{17}{360}\delta_\Delta^{3x}\right)\xi + \frac{1}{5}\delta_\Delta^{0} - \frac{1}{7}\delta_\Delta^{2x} + \frac{3}{35}\delta_\Delta^{4x}, \tag{19}$$

with

$$\begin{cases} \delta_\Delta^0 &= \tilde{w}(x_i - 2\Delta) + \tilde{w}(x_i - \Delta) + \tilde{w}(x_i) + \tilde{w}(x_i + \Delta) + \tilde{w}(x_i + 2\Delta), \\ \delta_\Delta^x &= -2\tilde{w}(x_i - 2\Delta) - \tilde{w}(x_i - \Delta) + \tilde{w}(x_i + \Delta) + 2\tilde{w}(x_i + 2\Delta), \\ \delta_\Delta^{2x} &= 2\tilde{w}(x_i - 2\Delta) - \tilde{w}(x_i - \Delta) - 2\tilde{w}(x_i) - \tilde{w}(x_i + \Delta) + 2\tilde{w}(x_i + 2\Delta), \\ \delta_\Delta^{3x} &= -6\tilde{w}(x_i - 2\Delta) + 12\tilde{w}(x_i - \Delta) - 12\tilde{w}(x_i + \Delta) + 6\tilde{w}(x_i + 2\Delta), \\ \delta_\Delta^{4x} &= \tilde{w}(x_i - 2\Delta) - 4\tilde{w}(x_i - \Delta) + 6\tilde{w}(x_i) - 4\tilde{w}(x_i + \Delta) + \tilde{w}(x_i + 2\Delta). \end{cases} \tag{20}$$

Note that δ_Δ^{4x} corresponds exactly to the estimate made in FAT of the fourth order spatial derivative of the displacement field (eq. 2). The bending curvature is,

$$\kappa_{x\,5}^{x_i}(\xi) = -\frac{1}{\Delta^2}\left(\frac{1}{2}\delta_\Delta^{4x}\xi^2 + \frac{1}{12}\delta_\Delta^{3x}\xi + \frac{1}{7}\delta_\Delta^{2x} - \frac{31}{84}\delta_\Delta^{4x}\right). \tag{21}$$

As shown in figure 1, the virtual segment is positioned on the sub-set of points between the points $\xi = -\tau$ and $\xi = \tau$ where $\tau \in [0, 2.5]$ since $M = 5$. The maximum value of τ is set to avoid extrapolation of the displacement field. The VFM is used to identify the applied dynamic force. The virtual displacement must meet the conditions detailed in the section 3. The virtual displacement is here based on the Hermite 16 interpolation functions which fulfill these conditions and have been used extensively in the past [12, 11]. These functions are defined piecewise on the virtual segment,

$$\begin{aligned} w^v(\xi) &= \frac{1}{4}\left(1 - \frac{2\xi}{\tau}\right)\left(2 + \frac{2\xi}{\tau}\right)^2 \text{ for } \xi \in [-\tau, 0], \\ w^v(\xi) &= \frac{1}{4}\left(1 + \frac{2\xi}{\tau}\right)\left(\frac{2\xi}{\tau} - 2\right)^2 \text{ for } \xi \in [0, \tau]. \end{aligned} \tag{22}$$

The virtual curvature is therefore,

$$\begin{aligned} \kappa_x^v(\xi) &= \frac{12}{\tau^3}\xi + \frac{6}{\tau^2} \text{ for } \xi \in [-\tau, 0], \\ \kappa_x^v(\xi) &= -\frac{12}{\tau^3}\xi + \frac{6}{\tau^2} \text{ for } \xi \in [0, \tau]. \end{aligned} \tag{23}$$

Virtual displacement and virtual curvature are shown in figure 2. In the case $M = 5$ and a virtual segment extending

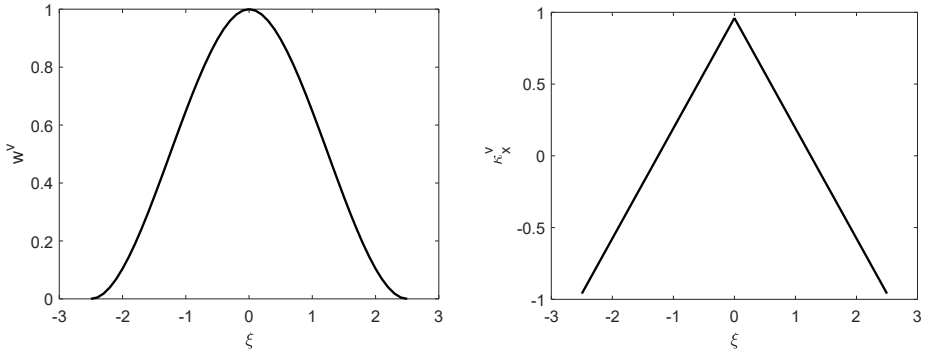

(a) (b)

Figure 2: (a) Virtual displacement w^v for $\tau = 2.5$ and (b) Virtual curvature κ_x^v for $\tau = 2.5$.

from $-\tau$ to $+\tau$, eq. 14 becomes,

$$\tilde{p}^{\text{VFM}}(x_i)\int_{-\tau}^{\tau} w^v(\xi)\mathrm{d}\xi = -\rho S\omega^2\int_{-\tau}^{\tau} W_5^{x_i}(\xi)w^v(\xi)\mathrm{d}\xi + EI\int_{-\tau}^{\tau}\kappa_{x\,5}^{x_i}(\xi)\kappa_x^v(\xi)\mathrm{d}\xi. \tag{24}$$

Using eqs. 19, 21, 22 and 23,

$$\begin{aligned} \tilde{p}^{\text{VFM}}(x_i) = -\rho S\omega^2(C_2\tilde{w}(x_i - 2\Delta) + C_1\tilde{w}(x_i - \Delta) + C_0\tilde{w}(x_i) + C_1\tilde{w}(x_i + \Delta) + C_2\tilde{w}(x_i + 2\Delta)) + \\ \frac{EI}{\Delta^4}[\tilde{w}(x_i - 2\Delta) - 4\tilde{w}(x_i - \Delta) + 6\tilde{w}(x_i) - 4\tilde{w}(x_i + \Delta) + \tilde{w}(x_i + 2\Delta)], \end{aligned} \tag{25}$$

where $C_2 = \left(\frac{\tau^4}{560} - \frac{\tau^2}{180}\right)$, $C_1 = \left(-\frac{\tau^4}{140} + \frac{4\tau^2}{45}\right)$ and $C_0 = \left(\frac{3\tau^4}{280} - \frac{\tau^2}{6} + 1\right)$.

4.3. Wavenumber analysis

The wavenumber transform of eq. 25 is,

$$\hat{p}^{\mathrm{VFM}}(k) = \imath\hat{w}(k)\left(EI(2\cos(2k\Delta) - 8\cos(k\Delta) + 6) - \rho S\omega^2(2C_2\cos(2k\Delta) + 2C_1\cos(k\Delta) + C_0)\right). \tag{26}$$

The VFM response can be estimated in the same way than FAT and CFAT using the error criterion,

$$E^{\mathrm{VFM}} = \frac{\hat{p}^{\mathrm{VFM}}(k)}{\hat{p}(k)} = \frac{\frac{1}{\Delta^4}(2\cos(2k\Delta) - 8\cos(k\Delta) + 6) - k_f^4(2C_2\cos(2k\Delta) + 2C_1\cos(k\Delta) + C_0))}{k^4 - k_f^4}. \tag{27}$$

Once again, this response has a singularity at the free bending wavenumber in the beam $k = k_f$. However, it is possible to remove this singularity by using the same principle as for CFAT. That is, by equalizing the roots of the numerator and denominator of eq. 27. In CFAT, this equalization is achieved through the correction factor μ^4 in eq. 8. In the VFM, this is achieved by adapting the size of the virtual τ segment in the PVW. Using $X = \cos(k\Delta)$, the numerator of eq. 27 becomes a quadratic function of X whose roots are the solutions of,

$$\frac{1}{\Delta^4}[4X^2 - 8X + 4] - k_f^4[4C_2X^2 + 2C_1X + C_0 - 2C_2]) = 0. \tag{28}$$

Introducing the number of points per wavelength, $n = 2\pi/k_f\Delta$, the roots are,

$$X_1 = \frac{6\,\pi^2\left(\sigma_1 + 14\,\tau^2\,\pi^2\right)}{-9\,\pi^4\,\tau^4 + 28\,\pi^4\,\tau^2 + 315\,n^4} + 1 \quad \text{and} \quad X_2 = 1 - \frac{6\,\pi^2\left(\sigma_1 - 14\,\tau^2\,\pi^2\right)}{-9\,\pi^4\,\tau^4 + 28\,\pi^4\,\tau^2 + 315\,n^4}, \tag{29}$$

where $\sigma_1 = \sqrt{-119\,\pi^4\,\tau^4 + 980\,\pi^4\,\tau^2 + 11025\,n^4}$. Figure 3 shows the roots X_1, X_2 as a function of n and for 3 different values of τ. The value $\tau = 0$ corresponds to a vanishingly small virtual segment. Apart from the singularity observed

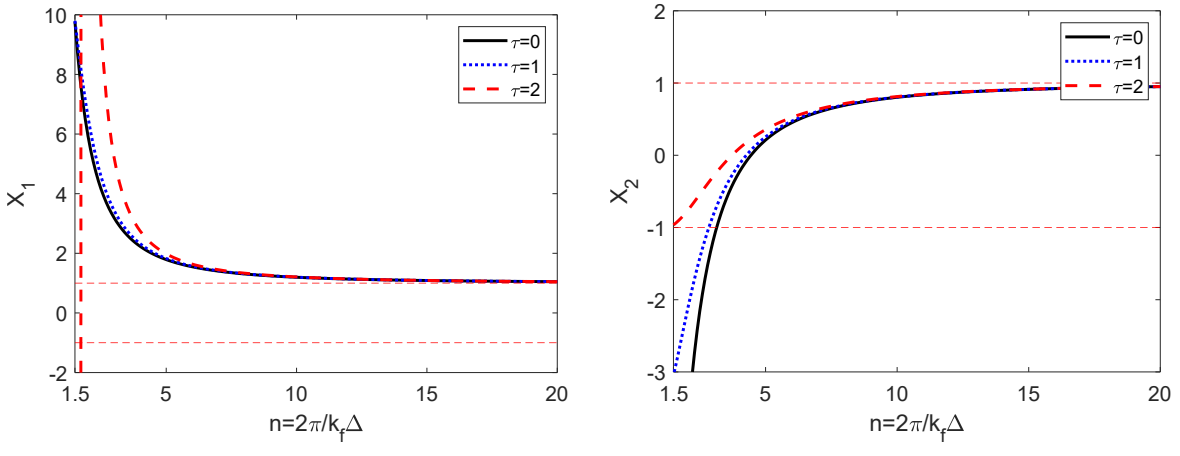

Figure 3: Roots of the numerator of eq. 27 for $\tau = 0$, $\tau = 1$ and $\tau = 2$ (a) X_1 and (b) X_2, the upper dashed red line corresponds to $X = 1$, the lower dashed red line corresponds to $X = -1$.

when $\tau = 2$ and $n = 1.8$, the root X_1 is always larger than 1. When $n \to \infty$, $X_1 \to 1^+$. Since $X = \cos(k\Delta)$, this root is not compatible with the problem. The root X_2 is mostly in the interval $[-1, 1]$ and is thus acceptable for our problem. When $n \to \infty$, $X_2 \to 1^-$. However, as τ and n decrease, the root becomes at some point smaller than -1. This limitation will be examined later. Keeping the root X_2, the size of the virtual segment τ, which ensures the equality of the roots of the numerator and denominator of eq. 27 is given by the equation,

$$1 - \frac{6\,\pi^2\left(\sigma_1 - 14\,\tau^2\,\pi^2\right)}{-9\,\pi^4\,\tau^4 + 28\,\pi^4\,\tau^2 + 315\,n^4} = \cos\left(k_f\Delta\right) = \cos\left(\frac{2\pi}{n}\right). \tag{30}$$

Equation 30 was solved using the Matlab® *symbolic toolbox*. Of the 8 roots obtained, only one is real and always stays in the interval $[0, 2.5]$ if n is not too small,

$$\tau_{\mathrm{FA}} = \frac{\sqrt{14\,\pi^2 \sin\left(\frac{\pi}{n}\right)^2 - 9\sqrt{35\,n^4 \sin\left(\frac{\pi}{n}\right)^4 + \frac{196\,\pi^4 \sin\left(\frac{\pi}{n}\right)^4}{81} + \frac{392\,\pi^4 \sin\left(\frac{\pi}{n}\right)^2}{27} - \frac{119\,\pi^4}{9}} + 42\,\pi^2}}{3\pi\left|\sin\left(\frac{\pi}{n}\right)\right|} \tag{31}$$

This value of τ is considered to be the Frequency Adapted (FA) virtual segment length in the VFM and is shown in figure 4. As n decreases, the Frequency Adapted value of τ at some point becomes larger than 2.5. Consequently, as

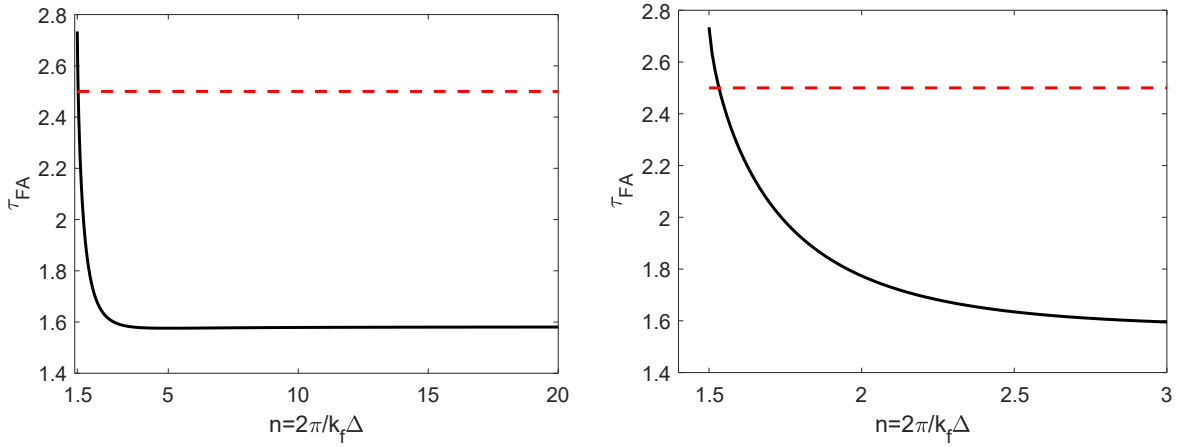

Figure 4: Frequency adapted value of the size τ of the virtual segment in the VFM (eq. 31) for (a) $n \in [1.5, 20]$ and (b) $n \in [1.5, 3]$. In both plots, the dotted horizontal red line represents the $\tau < 2.5$ limit.

mentioned above, the frequency adaptation process is limited at high frequency by the value of n. This limit will be discussed in section 4.4. The Frequency Adapted value does not depend strongly on n. Indeed, when n is larger than 3, τ_{FA} is quasi constant and equal to 1.58. This is an advantage of the frequency adaptation process. Indeed, n is a function of k_f, the flexural wavenumber of the beam, which in turn is a function of the structural parameter $EI/\rho S$. When the method is used to identify a dynamic force, the material is known and so is n a priori. The Frequency Adapted value of the size of the virtual segment can then be determined exactly using eq. 31. However, if the method is used to identify the structural parameter, the value of n remains unknown and so does the Frequency Adapted value of τ. The same problem is present in CFAT when it comes to estimating the corrective factor μ^4. For both techniques, a first solution to this problem is to perform a wavenumber analysis to obtain an initial estimate of k_f and therefore of n. CFAT and the Frequency-Adapted VFM can thus be applied to identify the structural parameter. An iterative process can then be carried out to obtain a better estimate of the value of n. For the VFM, a simpler approach is to use the observation made above that τ_{FA} according to n is almost constant. The Frequency-Adapted VFM can be applied with the average value of τ_{FA} in the interval $n \in [2, 20]$: $\tau_{\mathrm{FA}}^{\mathrm{mean}} = 1.58$, and no iterative process is required. Figure 5b shows the response of the VFM in the wavenumber domain for $n = 2.5$ and $n = 4$ without the frequency adaptation of the virtual segment length (here for $\tau = 0.5$) and with the frequency adaptation of the virtual segment length. The Frequency-Adapted VFM result is obtained using eq. 31 for the two values of n. The singularity at $k = k_f$ it completely removed when $\tau = \tau_{\mathrm{FA}}$. Once again, for $n = 2.5$, a second numerator root is visible at $k/k_f = 1.5$ for the Frequency-Adapted VFM plot. Note the similarity of FAT and the non-frequency-adapted VFM results on the one hand, and also of CFAT and the Frequency-Adapted VFM. In particular, there is a natural low-pass filtering of the VFM in the wave number domain which is due to the integration over the virtual segment in the PVW.

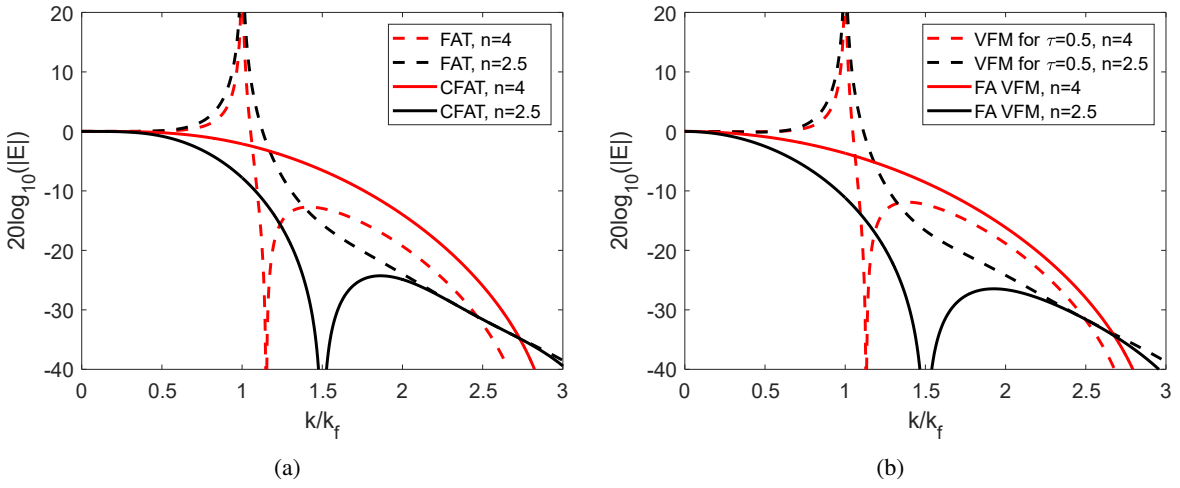

Figure 5: (a) Response of FAT and CFAT in the wavenumber domain for $n = 4$ and $n = 2.5$ as a function of k/k_f. The dashed lines correspond to FAT plots and the solid lines to the CFAT plots. (b) Response of the VFM for $\tau = 0.5$ and the Frequency-Adapted VFM in the wavenumber domain for $n = 4$ and $n = 2.5$ as a function of k/k_f. The dashed lines correspond to $\tau = 0.5$ and the solid lines to $\tau = \tau_{\text{FA}}$.

4.4. High frequency limit

In this section, the high-frequency limit of the VFM frequency adaptation process is examined. The first potential high-frequency limit is shown in figure 4. From this graph, it can be seen that as n becomes less than about 1.53, the frequency-adapted τ becomes larger than 2.5. However, as indicated in section 4.2, the maximum acceptable value of τ is 2.5. Consequently, the Frequency-Adapted VFM cannot be applied if $n > 1.53$. A second potential high frequency limit is given by the root X_2. Indeed, as indicated in section 4.3, the frequency adaptation of the virtual segment length in the VFM is valid when $X_2 \in [-1, 1]$. Since X_2 is a function of n and τ, the Frequency Adapted segment length given by eq. 31 is injected into eq. 29 so X_2 becomes only a function of n. The result is plotted in figure 6 for $n > 1.5$. The plot shows that X_2 for $\tau = \tau_{\text{FA}}$ is always in the interval $[-1, 1]$ for $n > 1.5$. This potential high-frequency limit

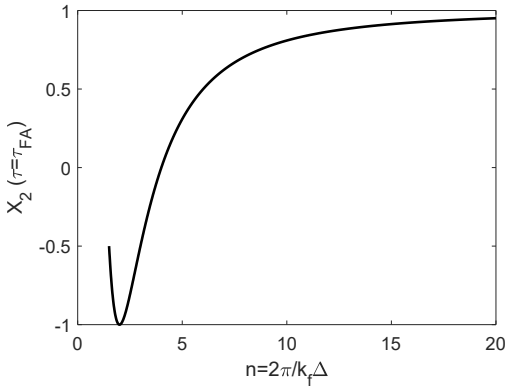

Figure 6: Root X_2 for $n \in [1.5, 20]$ and for $\tau = \tau_{\text{FA}}$.

on X_2 is therefore less restrictive than the condition $\tau < 2.5$. Another high-frequency limit is given by the Shannon criterion, which stipulates that the number of points per wavelength n must be larger than 2. However, this criterion is only valid for identifying the response of the structure and the structural parameter, since the bending wave number must first be identified as mentioned in section 4.3. In section 2, it was pointed out that for force identification, CFAT can be applied as long as $n > 1.85$ thanks to the anti-aliasing effect of the method. In [8], the limit $n > 1.85$ is set by keeping the magnitude of the secondary lobe of the wavenumber response below -10 dB. This lobe can be seen in figure 7 where the CFAT response for $n = 1.85$ is shown. With the Frequency-Adapted VFM, the magnitude of

Table 2
Coefficients U_l^{FAT}, U_l^{CFAT}, U_l^{VFM} and U_l^{VFM} for $\tau = 1.58$.

	U_0	U_1	U_2
FAT	$\frac{6EI}{\Delta^4} - \rho S\omega^2$	$-\frac{4EI}{\Delta^4}$	$\frac{EI}{\Delta^4}$
CFAT	$\frac{6EI}{\Delta^4}\mu^4 - \rho S\omega^2$	$-\frac{4EI}{\Delta^4}\mu^4$	$\frac{EI}{\Delta^4}\mu^4$
VFM	$\frac{6EI}{\Delta^4} - \rho S\omega^2\left(\frac{3\tau^4}{280} - \frac{\tau^2}{6} + 1\right)$	$-\frac{4EI}{\Delta^4} - \rho S\omega^2\left(-\frac{\tau^4}{140} + \frac{4\tau^2}{45}\right)$	$\frac{EI}{\Delta^4} - \rho S\omega^2\left(\frac{\tau^4}{560} - \frac{\tau^2}{180}\right)$
VFM $(\tau = \tau_{\text{FA}}^{\text{mean}})$	$\frac{6EI}{\Delta^4} - 0.65\rho S\omega^2$	$-\frac{4EI}{\Delta^4} - 0.17\rho S\omega^2$	$\frac{EI}{\Delta^4} + 0.0027\rho S\omega^2$

the secondary lobe exceeds -10 dB when n falls below 1.65. The Frequency-Adapted VFM wavenumber response for $n = 1.65$ is also shown in figure 7. Therefore, for force identification, the Frequency-Adapted VFM can be applied as

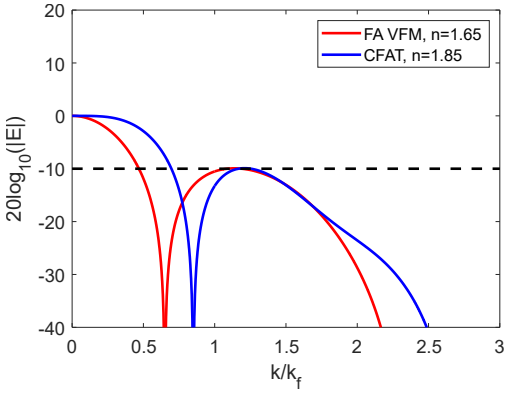

Figure 7: Response of CFAT in the wavenumber domain for $n = 1.85$; Response of the Frequency-Adapted VFM for $n = 1.65$ as a function of k/k_f. The horizontal black line represents the limit of -10 dB.

long as $n > 1.65$.

4.5. Comparison of the VFM with FAT and CFAT

At this point, it is useful to explicitly write the identified external load $\tilde{p}$ as a function of the nodal displacements for the different methods. To do so eq. 25 can be rewritten as,

$$\tilde{p}^{\text{VFM}}(x_i) = U_0^{\text{VFM}}\tilde{w}(x_i) + \sum_{l=1}^{2} U_l^{\text{VFM}}(\tilde{w}(x_i - l\Delta) + \tilde{w}(x_i + l\Delta)) \tag{32}$$

where, U_l^{VFM} are the coefficients deduced from eq. 25. The same development can be done for FAT and CFAT using eqs. 3 and 7 in order to introduce the corresponding coefficients U_l^{FAT} and U_l^{CFAT} respectively. The various coefficients are shown in Table 2. The last line is obtained by using the averaged value of τ_{FA} in the interval $n \in [2, 20]$ introduced in section 4.3, $\tau_{\text{FA}}^{\text{mean}} = 1.58$. First, it should be noted that the VFM formalism induces a smoothing effect in the estimation of the inertial term. This effect is demonstrated by the presence of the inertial term in U_1 and U_2 of the VFM, whereas it is absent in the FAT or CFAT coefficients. This highlights the different strategies adopted by CFAT and the VFM to deal with low values of n: CFAT corrects the finite difference scheme and thus acts directly on the rigidity term. The VFM smoothes the considered field in the inertia term, thus balancing the low-pass effect of finite differences. These two strategies, although fundamentally different, lead to surprisingly similar performances. Now and hereafter, a simply supported beam composed of steel, $\rho = 7800$ kg/m^3 and $E = 210$ GPa, is considered. The cross section is $S = 5 \times 10^{-5}$ m^2 and the flexural moment of inertia is $I = 1 \times 10^{-10}$ m^4. Figure 8 shows a comparison of the U_0, U_1, U_2 coefficients for the different methods and for $n = 4$ and $n = 2.5$ as a function of τ. At $\tau \simeq 0.29$, U_0^{VFM} is close to zero, this explains the observed dip on figure 8a. When $\tau = 0$, the U_l^{VFM} are equal to U_l^{FAT}. In other words, both methods are equivalent for a vanishingly small virtual segment. The CFAT plots for $n = 4$ (Figure 8b) show that when

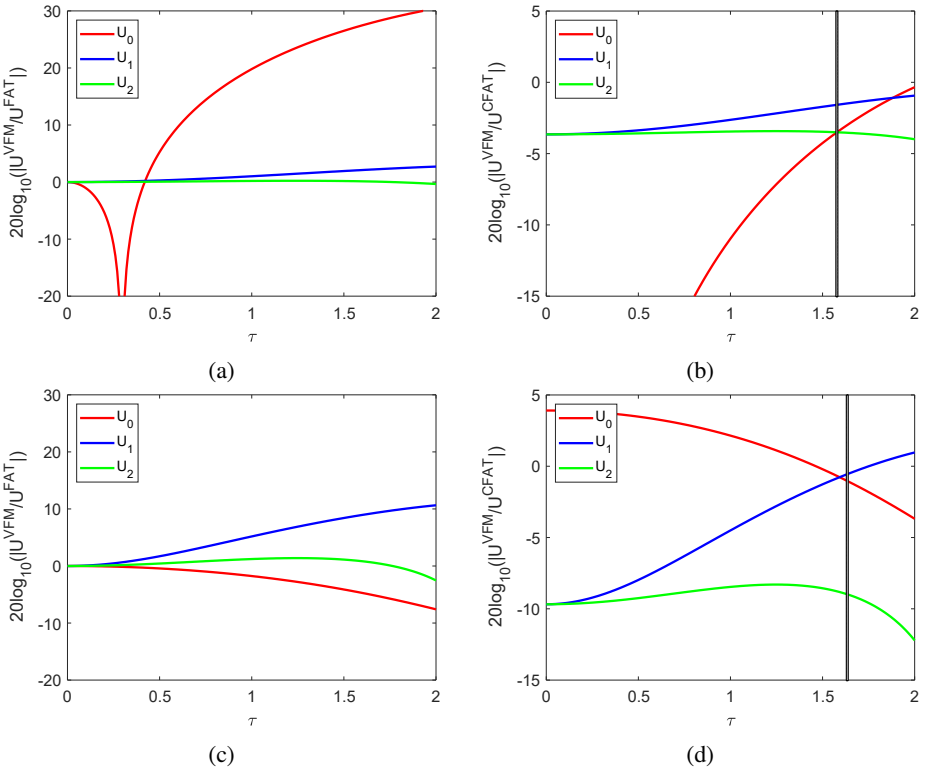

Figure 8: (a) Coefficients U^{VFM} in dB (ref: U^{FAT}) for $n = 4$, as a function of τ, (b) Coefficients U^{VFM} in dB (ref: U^{CFAT}) for $n = 4$, (c) Coefficients U^{VFM} in dB (ref: U^{FAT}) for $n = 2.5$, (d) Coefficients U^{VFM} in dB (ref: U^{CFAT}) for $n = 2.5$. The black vertical lines in the CFAT plots correspond to τ_{FA}.

$\tau = \tau_{\text{FA}}$ the difference between the coefficients U^{VFM} and U^{CFAT} is relatively small. So, even though the difference is smaller as τ increases, this means once again that both methods are almost equivalent for $\tau = \tau_{\text{FA}}$. However, for $n = 2.5$ (Figure 8d) the difference between U_2^{VFM} and U_2^{CFAT} is significant while the difference between U_1^{VFM} and U_1^{CFAT} (or U_0^{VFM} and U_0^{CFAT}) remains reasonably small. Figure 9a plots the coefficients U_0^{CFAT}, U_1^{CFAT} and U_2^{CFAT} as a function of n. Figure 9b shows the same plots for the Frequency-Adapted VFM. These plots show that in the high

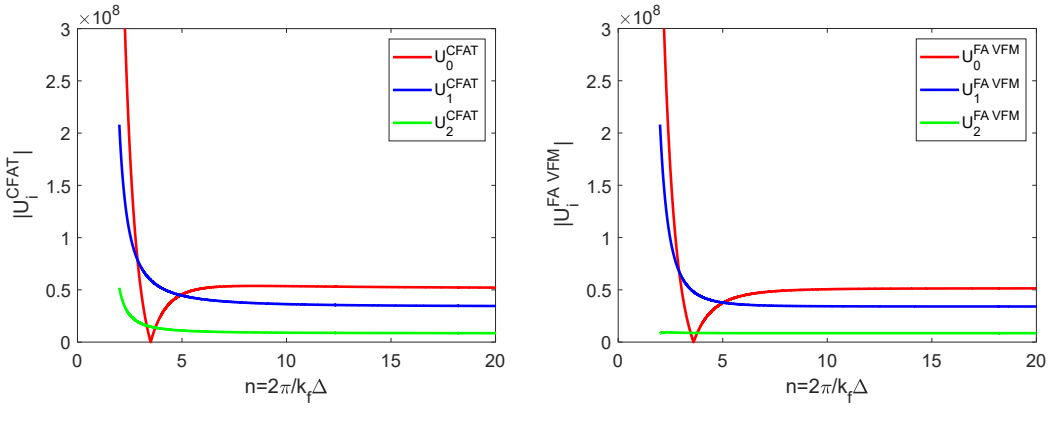

Figure 9: (a) U_0^{CFAT}, U_1^{CFAT} and U_2^{CFAT} as a function of $n = \frac{2\pi}{k_f \Delta}$, (b) $U_0^{\text{FA VFM}}$, $U_1^{\text{FA VFM}}$ and $U_2^{\text{FA VFM}}$.

frequency domain (n small), the coefficient U_2 is negligible compared to U_1 and U_0. Therefore, the large discrepancy observed in figure 8d is inconsequential and the conclusions drawn for $n = 4$ can also be drawn for $n = 2.5$.

5. Numerical Results

5.1. Direct problem

Consider a simply supported beam, subjected to a harmonic force of angular frequency ω and amplitude 1 N at $x = x_e$. Structural dissipation is taken into account using a complex Young Modulus $\tilde{E} = E(1 + j\eta)$. The transverse displacement is simulated using the modal expansion [8],

$$\tilde{w}(x) = \frac{2}{\tilde{E} I L} \sum_{r=1}^{N} \frac{\sin(x_e \frac{r\pi}{L}) \sin(x \frac{r\pi}{L})}{\left(\frac{r\pi}{L}\right)^4 - k_f^4} \tag{33}$$

where L is the length of the beam. The simulated beam is similar to the one considered in section 4.5 ($\rho = 7800$ kg/m^3, $E = 210$ GPa, $S = 5 \times 10^{-5}$ m^2 and $I = 1 \times 10^{-10}$ m^4). The loss factor is $\eta = 5\%$. The length of the beam is $L = 1$ m. The force position is $x_e = 0.2$ m. The spatial sampling is $\Delta = 0.04$ m. Using the simulated displacement at each point, a white Gaussian noise with an SNR of 30dB is added to the simulated displacement. The noisy displacement field at ω is calculated using the following formula:

$$\tilde{w}_{\text{noisy}}(x) = \tilde{w}(x) + N_r \sigma_w 10^{-\text{SNR}/20} \tag{34}$$

where N_r is a random variable sampled from a standard normal distribution and σ_w is the standard deviation of the simulated displacement at ω. When the methods are used to identify a dynamic force, the simulation is computed for $f \in [10, 10800]$ Hz which correspond to $n \in [54, 1.65]$ for the chosen spatial sampling. When the methods are used to identify a structural parameter, the simulation is computed for $f \in [10, 7300]$ Hz which correspond to $n \in [54, 2]$. The number of modes N is chosen so that the highest eigen frequency is at least 10 times greater than the high-frequency limit.

5.2. Inverse problem for force identification

FAT, CFAT, the VFM for $\tau = 0.5$ and the Frequency-Adapted VFM are used to locate and quantify the force applied on the beam. The VFM for $\tau = 0.5$ and the Frequency-Adapted VFM are applied for $n \in [54, 1.65]$ while FAT and CFAT are applied for $n \in [54, 1.85]$ to respect the high-frequency limits developed in section 4.4. In the Frequency-Adapted VFM, the Frequency Adapted value of τ is calculated for each value of n using eq. 31. The lineic force obtained with each method is shown in figure 10 as a function of position x along the beam and number of points per bending wavelength n (increasing values of n correspond to decreasing values of the frequency ω). The bias error due to the finite difference scheme approximation strongly deteriorates the FAT results. However the force is correctly localized in low frequencies. The VFM results obtained when $\tau = 0.5$ are similar to the ones obtained with FAT. The effects of the CFAT correction and of the VFM frequency adaptation are well observable on the bottom plots of figure 10. The Frequency-Adapted VFM result is less noisy than the CFAT result. This is due to the integration on the virtual segment which acts as low-pass wavenumber filter. The identified lineic force is then integrated over the interval $[0.2 - \Delta, 0.2 + \Delta]$, which is the smallest possible interval centered on the point of force. It consists of the point load and the two points surrounding it. This operation yields a force value. Figure 11 shows the force spectra obtained after this spatial integration with all methods. The expected value is 0 dB (1N point load). In low frequencies (when n is large) all methods are inaccurate because of measurement noise. The errors of CFAT and of the Frequency-Adapted VFM remain less than 3.3 dB when $n < 4$ while the results obtained with FAT and the VFM when $\tau = 0.5$ or $\tau = 2$ show large errors. When $n < 2$, the CFAT results remain accurate. With the Frequency-Adapted VFM, as n decreases, the results become almost equivalent to those obtained with VFM for $\tau = 2$ and the identified load becomes underestimated. This is due to the fact that the length of the frequency-adapted virtual segment becomes larger, and the low-pass filtering effect becomes more important.

5.3. Inverse problem for structural parameter identification

As stated in the sections 2 and 3 the methods can be used to identify the structural parameter of the beam $EI/\rho S = 56.1$ m^4.s^{-2}. The condition is that the external force at point x where the methods are applied is zero.

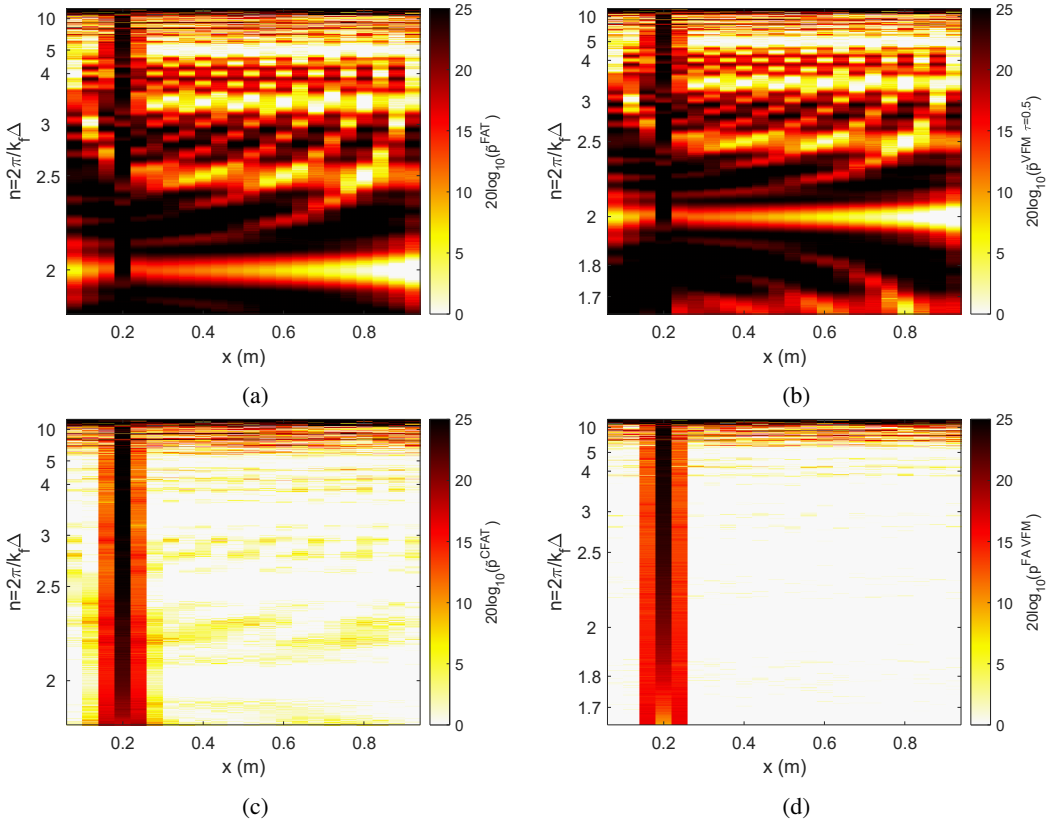

Figure 10: (a) Lineic force identified with the FAT in dB (ref: 1N/m) as a function of position along the beam and number of points per wavelength n, (b) Lineic force identified with the VFM for $\tau = 0.5$, (c) Lineic force identified with CFAT, (d) Lineic force identified with the Frequency-Adapted VFM using eq. 31.

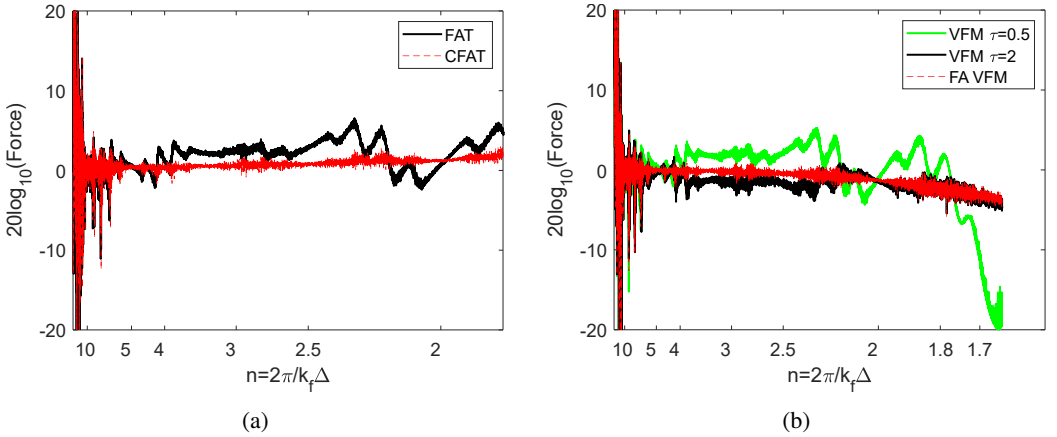

Figure 11: (a) Force spectra identified with FAT and CFAT in dB (ref : 1 N) (b) Force spectra identified with the VFM with $\tau = 0.5$ and with $\tau = 2$ and the Frequency-Adapted VFM in dB (ref : 1 N).

The methods are applied by placing the force at $x_e = 0.04$ m. The structural parameter is identified for each value of n using least-squares estimation. This estimation is performed using spatial points far from force application point. In total 23 measurement points distributed between the point with coordinate $x = 0.12$ m and the end of the beam are used. Figure 12 shows the structural parameter identified with FAT, CFAT, the VFM when $\tau = 0.5$ and the

Frequency-Adapted VFM as a function of n. Here, the number of points per wavelength n is considered as known a priori. Therefore, the Frequency Adapted length of the virtual segment is directly computed using eq. 31. The μ^4 correction factor can also be calculated directly to apply CFAT. At low frequencies, all methods underestimate the

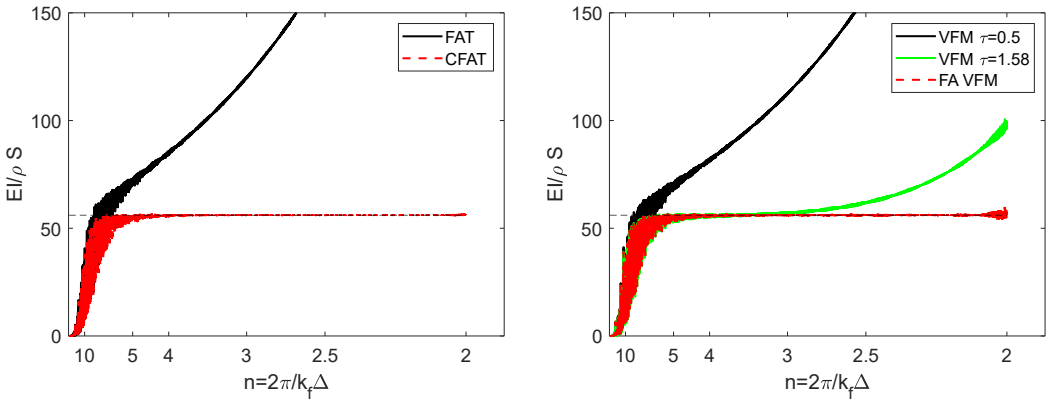

Figure 12: (a) Structural parameter identified with FAT and CFAT as a function of the number of points per wavelength n, (b) Structural parameter identified with the VFM for $\tau = 0.5$, the VFM for $\tau = 1.58$ and the Frequency-Adapted VFM using eq. 31 as a function of the number of points per wavelength n. In both plots, the horizontal dotted black line represents the reference value.

structural parameter. This result can be explained by the fact that when n is large, the spacing between measurement points becomes very small compared to the wavelength, and consequently the spatial derivatives of the displacement field becomes very sensitive to the measurement noise present in the simulations. The structural parameter identified with FAT and the VFM when $\tau = 0.5$ is overestimated at most frequencies and the error increases with the frequency. CFAT and the Frequency-Adapted VFM perform well at most frequencies. The accuracy of the CFAT correction and of the VFM frequency adaptation is once again demonstrated.
In practice, when the Frequency-Adapted VFM is applied to identify $EI/\rho S$, the number of points per wavelength n remains unknown since the bending wavelength depends on $EI/\rho S$. As detailed in section 4.3, this problem can be solved using an average value of the Frequency Adapted value of the size τ of the virtual segment $\tau_{\mathrm{FA}}^{\mathrm{mean}}$ equal to 1.58. The structural parameter identified with the Frequency-Adapted VFM using this average value of τ_{FA} is shown in the figure 12b. The result obtained with the VFM for $\tau = \tau_{\mathrm{FA}}^{\mathrm{mean}}$ is almost similar to the one obtained with the Frequency-Adapted VFM in the low and medium frequencies. The most important difference is obtained in the high frequency domain because, at this point $\tau_{\mathrm{FA}}^{\mathrm{mean}}$ becomes quite different to the exact value of τ_{FA}.

5.4. Sensitivity to measurement noise

The sensitivity of the VFM to measurement noise has previously been studied to help construct special virtual fields used to identify structural parameters [18, 22]. However, unlike the virtual fields used in this study, special virtual fields are functions of the vibratory field and must therefore be calculated at each frequency. In this section, the noise sensitivity of CFAT and the Frequency-Adapted VFM is studied for the identification of force and structural parameters. When a force is identified, a distinction is made between two regions where results are presented. The first region is located around the point of application of the force $[x_e - \Delta, x_e + \Delta]$ and the second region is the remaining part of the beam. The noise sensitivity S_f of the methods is given by the ratio of the integrated squared residual force outside the interval $[x_e - \Delta, x_e + \Delta]$ with the square of the integrated lineic force around the point load:

$$S_f = \frac{\displaystyle\int_0^{x_e-\Delta} \left|\tilde{p}^{\mathrm{id}}(x)\right|^2 \mathrm{dx} + \int_{x_e+\Delta}^{L} \left|\tilde{p}^{\mathrm{id}}(x)\right|^2 \mathrm{dx}}{\left|\displaystyle\int_{x_e-\Delta}^{x_e+\Delta} \tilde{p}^{\mathrm{id}}(x)\mathrm{dx}\right|^2}. \tag{35}$$

Therefore, S_f, compares the magnitude of the reconstructed force (denominator term) with the average magnitude of the residual forces (numerator term). Figure 13 shows S_f as a function of n for CFAT and the Frequency-Adapted VFM and for an SNR of 30dB and one of 10dB. In each figure, the sensitivity of the methods when no measurement noise is added to the simulation is also shown, in order to demonstrate the systematic error of each method, caused by spatial sampling and polynomial fitting. When SNR is 30dB and in the low frequencies ($n > 10$), S_f is high, so the

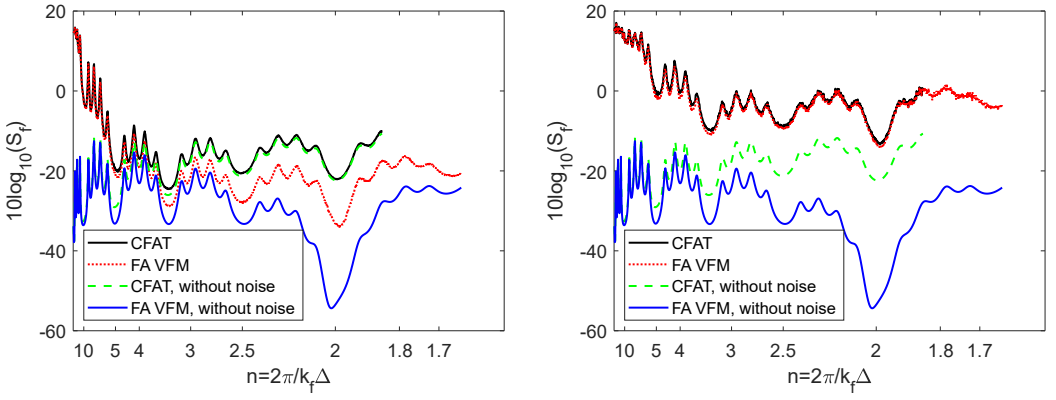

Figure 13: (a) Sensitivity S_f of CFAT and the Frequency-Adapted VFM to measurement noise for a SNR of 30dB as a function of n (b) Sensitivity S_f of CFAT and the Frequency-Adapted VFM to measurement noise for a SNR of 10dB as a function of n.

results are dominated by noise. At mid and high frequencies ($n < 10$), S_f takes smaller values and results are therefore less dominated by noise. The S_f values obtained with the Frequency-Adapted VFM are smaller than those of CFAT, which means that the residual force identified is less significant. These results are in line with the plots in figures 10 and 11. When the SNR is 10 dB, S_f remains high at most frequencies, showing that the results are mainly dominated by noise. The sensitivity of CFAT and of the Frequency-Adapted VFM for identifying structural parameters is defined here using the standard deviation σ of the identified structural parameter $EI/\rho S$. At each frequency point, the standard deviation is calculated using 23 points distributed between the $x = 0.12$ m coordinate point and the end of the beam. The $x = 0.12$ m coordinate point is chosen so that the results are not disturbed by the source placed at $x_e = 0.04$ m. The standard deviation obtained is normalized by the mean value of the identified structural parameter. Figure 14 shows the standard deviation calculated for CFAT and the Frequency-Adapted VFM as a function of n and once again for two SNR values: 30 dB and 10 dB. When the SNR is 30 dB, the standard deviation is high in the low frequencies ($n > 10$).

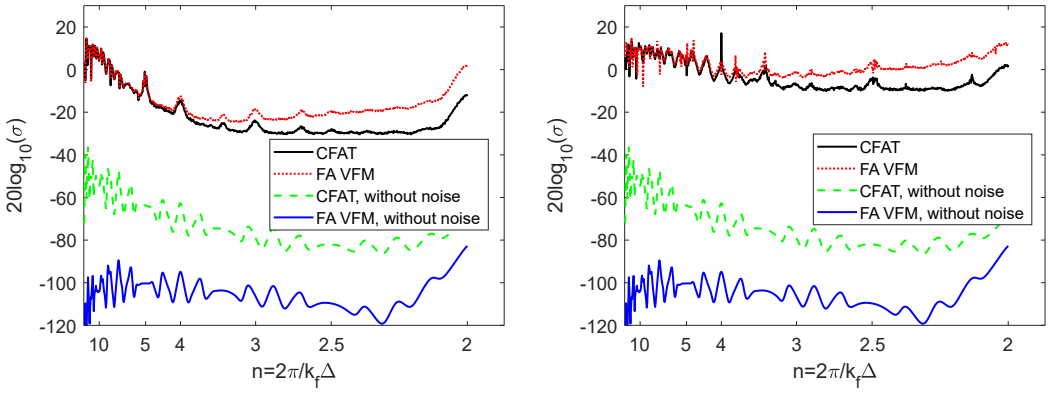

Figure 14: (a) Normalized standard deviation $\sigma^{\text{norm.}}$ of CFAT and the Frequency-Adapted VFM in dB for a SNR of 30dB as a function of n (b) Normalized standard deviation $\sigma^{\text{norm.}}$ of CFAT and the Frequency-Adapted VFM in dB for a SNR of 10dB as a function of n.

This indicates that the results are very noisy. However, the value of σ decreases with n, showing the improvement in results as frequency increases. These observations are consistent with Figure 12. When the SNR is 10 dB, the standard deviation is high at most frequencies. The results are then dominated by noise. In the high-frequency domain ($n < 4$), Frequency-Adapted VFM is more sensitive to noise than CFAT when identifying a structural parameter. Overall, whether for the identification of structural parameters or dynamic forces, CFAT and the Frequency-Adapted VFM appear to have almost equivalent sensitivity to measurement noise. Because it is based on a weak formulation of the beam equilibrium and it involves lower order spatial derivatives of the measured displacement field as compared to the strong formulation, the VFM should be less sensitive to measurement noise. A first explanation to our observations on noise sensitivity of the two methods is that the case of the Euler-Bernouilli beam is less favourable than the case of the Love-Kirchhoff plate, since a smaller number of measurement points are used on the virtual segment as compared to a virtual surface for a plate. A second explanation is that, as a result of the developments made, the Frequency-Adapted VFM formalism is very close to that of CFAT.

6. Conclusion

This paper has presented the frequency adaptation of the Virtual Fields Method for the identification of dynamic forces and structural parameters in the case of a homogeneous and isotropic bending beam. The VFM requires choosing a test function called virtual field to solve the principle of virtual work. The frequency adaptation of the method is performed using polynomial interpolation of the displacement field and the same principle that led to the correction of the Force Analysis Technique (the Corrected Force Analysis Technique). In the VFM, the virtual fields are defined here over a virtual segment over which the unknown external load or structural parameters are searched. Like FAT, the VFM response shows a singularity at the free bending wavenumber of the beam. The frequency adaptation of the method consists in calculating the length of the virtual segment which will allow to compensate this singularity for each value of the number of discrete measurement points per wavelength. Numerical simulations have shown that the Frequency-Adapted VFM provides good results in the high frequency domain for both force and structural parameter identification. In future work, the Frequency-Adapted VFM will be extended to plates and tested on experimental data.

Acknowledgement

This study was funded by the Fonds de recherche du Québec - Nature et technologies (FRQNT) and was performed within the framework of the Labex CeLyA of Université de Lyon, operated by the French National Research Agency (ANR-10-LABX- 0060/ ANR-11-IDEX0007).

References

[1] Kerem Ege, Xavier Boutillon, and Bertrand David. “High-resolution modal analysis”. en. In: Journal of Sound and Vibration 325 (Sept. 2009), pp. 852–869. DOI: 10.1016/j.jsv.2009.04.019. URL: https://linkinghub.elsevier.com/retrieve/pii/S0022460X09003447.

[2] Fabien Marchetti. “Modélisation et caractérisation large bande de plaques multicouches anisotropes”. fr. PhD thesis. Lyon, France: Institut National des Sciences Appliquées de Lyon, Dec. 2019. URL: https://www.researchgate.net/publication/338736309_Modelisation_et_caracterisation_large_bande_de_plaques_multicouches_anisotropes.

[3] Charles Pezerat and Jean-Louis Guyader. “Two inverse methods for localization of external sources exciting a beam”. In: Acta Acustica 3 (Feb. 1995), pp. 1–10. URL: https://www.researchgate.net/publication/275657452_Two_inverse_methods_for_localization_of_external_sources_exciting_a_beam.

[4] Charles Pezerat and Jean-Louis Guyader. “Identification of vibration sources”. en. In: Applied Acoustics 61 (Nov. 2000), pp. 309–324. DOI: 10.1016/S0003-682X(00)00036-0. URL: https://www.sciencedirect.com/science/article/pii/S0003682X00000360.

[5] Frédéric Ablitzer, Charles Pézerat, Jean-Michel Génevaux, and Jérôme Bégué. “Identification of stiffness and damping properties of plates by using the local equation of motion”. en. In: Journal of Sound and Vibration 333 (Apr. 2014), pp. 2454–2468. DOI: 10.1016/j.jsv.2013.12.013. URL: https://linkinghub.elsevier.com/retrieve/pii/S0022460X13010535.

[6] Frédéric Ablitzer, Charles Pézerat, Bertrand Lascoup, and Julien Brocail. “Identification of the flexural stiffness parameters of an orthotropic plate from the local dynamic equilibrium without a priori knowledge of the principal directions”. en. In: Journal of Sound and Vibration 404 (Sept. 2017), pp. 31–46. DOI: 10.1016/j.jsv.2017.05.037. URL: https://linkinghub.elsevier.com/retrieve/pii/S0022460X1730425X.

[7] Quentin Leclère, Frédéric Ablitzer, and Charles Pézerat. “Practical implementation of the corrected force analysis technique to identify the structural parameter and load distributions”. en. In: Journal of Sound and Vibration 351 (Sept. 2015), pp. 106–118. DOI: 10.1016/j.jsv.2015.04.025. URL: https://linkinghub.elsevier.com/retrieve/pii/S0022460X15003570.

[8] Quentin Leclère and Charles Pézerat. “Vibration source identification using corrected finite difference schemes”. en. In: Journal of Sound and Vibration 331 (Mar. 2012), pp. 1366–1377. DOI: 10.1016/j.jsv.2011.11.002. URL: https://linkinghub.elsevier.com/retrieve/pii/S0022460X11008807.

[9] Fabien Marchetti, Kerem Ege, and Quentin Leclère. “Development of the Corrected Force Analysis Technique for laminated composite panels”. en. In: Journal of Sound and Vibration 490 (Jan. 2021), p. 115692. DOI: 10.1016/j.jsv.2020.115692. URL: https://linkinghub.elsevier.com/retrieve/pii/S0022460X20305228.

[10] Kerem Ege, N.B. Roozen, Quentin Leclère, and Renaud G. Rinaldi. “Assessment of the apparent bending stiffness and damping of multilayer plates; modelling and experiment”. en. In: Journal of Sound and Vibration 426 (July 2018), pp. 129–149. DOI: 10.1016/j.jsv.2018.04.013. URL: https://linkinghub.elsevier.com/retrieve/pii/S0022460X18302384.

[11] Fabrice Pierron and Michel Grédiac.
The Virtual Fields Method: Extracting Constitutive Mechanical Parameters from Full-field Deformation Measurements. en. New York: Springer-Verlag, 2012. ISBN: 978-1-4614-1823-8. DOI: 10.1007/978-1-4614-1824-5. URL: https://www.springer.com/gp/book/9781461418238.

[12] Alain Berry, Olivier Robin, and Fabrice Pierron. “Identification of dynamic loading on a bending plate using the Virtual Fields Method”. en. In: Journal of Sound and Vibration 333 (Dec. 2014), pp. 7151–7164. DOI: 10.1016/j.jsv.2014.08.038. URL: https://linkinghub.elsevier.com/retrieve/pii/S0022460X1400710X.

[13] Alain Berry and Olivier Robin. “Identification of spatially correlated excitations on a bending plate using the Virtual Fields Method”. en. In: Journal of Sound and Vibration 375 (Aug. 2016), pp. 76–91. DOI: 10.1016/j.jsv.2016.03.042. URL: https://linkinghub.elsevier.com/retrieve/pii/S0022460X16300177.

[14] Patrick O’Donoughue, Olivier Robin, and A. Berry. “Time-resolved identification of mechanical loadings on plates using the virtual fields method and deflectometry measurements”. en. In: Strain 54 (June 2018), e12258. DOI: 10.1111/str.12258. URL: https://onlinelibrary.wiley.com/doi/10.1111/str.12258.

[15] Patrick O’Donoughue, Olivier Robin, and Alain Berry. “Time-space identification of mechanical impacts and distributed random excitations on plates and membranes”. In:
Proceedings of the Institution of Mechanical Engineers, Part C: Journal of Mechanical Engineering Science 233 (Sept. 2019), pp. 6436–6447. DOI: 10.1177/0954406219839094. URL: https://doi.org/10.1177/0954406219839094.

[16] Alain Giraudeau and Fabrice Pierron. “Identification of stiffness and damping properties of thin isotropic vibrating plates using the virtual fields method: theory and simulations”. en. In: Journal of Sound and Vibration 284 (June 2005), pp. 757–781. DOI: 10.1016/j.jsv.2004.07.009. URL: http://www.sciencedirect.com/science/article/pii/S0022460X04006091.

[17] Alain Giraudeau and Fabrice Pierron. “Identification of material stiffness and damping in vibrating plates using full-field measurements”. en. In: Journal of Physics: Conference Series 181 (Aug. 2009), p. 012063. DOI: 10.1088/1742-6596/181/1/012063. URL: https://doi.org/10.1088%2F1742-6596%2F181%2F1%2F012063.

[18] Michel Grédiac, Evelyne Toussaint, and Fabrice Pierron. “Special virtual fields for the direct determination of material parameters with the virtual fields method. 1—Principle and definition”. en. In: International Journal of Solids and Structures 39 (May 2002), pp. 2691–2705. DOI: 10.1016/S0020-7683(02)00127-0. URL: http://www.sciencedirect.com/science/article/pii/S0020768302001270.

[19] Michel Grédiac, Evelyne Toussaint, and Fabrice Pierron. “Special virtual fields for the direct determination of material parameters with the virtual fields method. 2—Application to in-plane properties”. en. In: International Journal of Solids and Structures 39 (May 2002), pp. 2707–2730. DOI: 10.1016/S0020-7683(02)00128-2. URL: http://www.sciencedirect.com/science/article/pii/S0020768302001282.

[20] Michel Grédiac, Evelyne Toussaint, and Fabrice Pierron. “Special virtual fields for the direct determination of material parameters with the virtual fields method. 3. Application to the bending rigidities of anisotropic plates”. en. In: International Journal of Solids and Structures 40 (May 2003), pp. 2401–2419. DOI: 10.1016/S0020-7683(03)00030-1. URL: http://www.sciencedirect.com/science/article/pii/S0020768303000301.

[21] Chanyang Kim, Jin-Hwan Kim, and Myoung-Gyu Lee. “A virtual fields method for identifying anisotropic elastic constants of fiber reinforced composites using a single tension test: Theory and validation”. en. In: Composites Part B: Engineering 200 (Nov. 2020), p. 108338. DOI: 10.1016/j.compositesb.2020.108338. URL: https://linkinghub.elsevier.com/retrieve/pii/S1359836820333874.

[22] S. Avril, M. Grédiac, and F. Pierron. “Sensitivity of the virtual fields method to noisy data”. en. In: Computational Mechanics 34 (Nov. 2004). Number: 6, pp. 439–452. DOI: 10.1007/s00466-004-0589-6. URL: http://link.springer.com/10.1007/s00466-004-0589-6.

[23] Alain Giraudeau, Fabrice Pierron, and Baoqiao Guo. “An alternative to modal analysis for material stiffness and damping identification from vibrating plates”. en. In: Journal of Sound and Vibration 329 (May 2010), pp. 1653–1672. DOI: 10.1016/j.jsv.2009.11.031. URL: https://linkinghub.elsevier.com/retrieve/pii/S0022460X09009754.

[24] Aleksander Marek, Frances M. Davis, and Fabrice Pierron. “Sensitivity-based virtual fields for the non-linear virtual fields method”. en. In: Computational Mechanics 60 (Sept. 2017). Number: 3, pp. 409–431. DOI: 10.1007/s00466-017-1411-6. URL: http://link.springer.com/10.1007/s00466-017-1411-6.

[25] N. Connesson, E. H. Clayton, P. V. Bayly, and F. Pierron. “Extension of the Optimised Virtual Fields Method to Estimate Viscoelastic Material Parameters from 3D Dynamic Displacement Fields”. en. In: Strain 51.2 (Apr. 2015), pp. 110–134. ISSN: 0039-2103, 1475-1305. DOI: 10.1111/str.12126. URL: https://onlinelibrary.wiley.com/doi/10.1111/str.12126 (visited on 11/10/2023).

[26] Mariano Gasca and Thomas Sauer. “Polynomial interpolation in several variables”. en. In: Advances in Computational Mathematics 12 (Mar. 2000), pp. 377–410. DOI: https://doi.org/10.1023/A:1018981505752. URL: https://link.springer.com/article/10.1023/A:1018981505752.